

# Effects of Wall Heat Loss on Swirl-Stabilized Nonpremixed Flames With Localized Extinction

Huangwei Zhang<sup>1</sup>

Department of Mechanical Engineering,  
National University of Singapore,  
9 Engineering Drive 1,  
Singapore 117576  
e-mail: huangwei.zhang@nus.edu.sg

*Large eddy simulation (LES) with three-dimensional conditional moment closure (CMC) subgrid model for combustion is applied to simulate a swirl-stabilized nonpremixed methane flame with localized extinction, with special focus on the effects of heat loss to the burner surface. The convective wall heat loss is modeled through introducing a source term in the conditionally filtered total enthalpy equation for the CMC cells adjacent to the wall. The mean heat flux is high on the middle surface of the bluff body, but relatively low near its edges. The turbulent heat flux based on the gradient of the resolved temperature is relatively low compared to the laminar counterpart, but increases with the turbulent intensity. The heat loss facilitates the occurrences of extinction and re-ignition for the CMC cells immediately adjacent to the wall, evidenced by comparing flame structures in the near-wall CMC cells. This can be directly linked to the increase of the mean conditional scalar dissipation near the wall in the heat loss case. Furthermore, the degree of local extinction near the bluff body measured by conditional reactedness at stoichiometry is intensified due to the wall heat loss. However, the results also show that there is negligible influence of wall heat loss on the probability density function (PDF) of the lift-off height, demonstrating the dominance of aerodynamic effects on flame stabilization. The results are in reasonable agreement with experimental measurements.*

[DOI: 10.1115/1.4040516]

*Keywords:* swirl nonpremixed flames, wall heat loss, local extinction, large eddy simulations, conditional moment closure

## 1 Introduction

Flame–wall interaction is a physicochemical process in which flames and wall surfaces affect each other through the coupling of chemical kinetics, momentum, and heat transfer [1]. For instance, when flame fronts approach the vicinity of walls or propagate in tubes, the former are cooled and the latter are heated with strong heat fluxes, accompanied by the variations of near-wall flame reactivity and flow properties like density and viscosity. Flame–wall interactions exist in meso- and microscale combustion devices [2,3], laboratory burners [1], industrial combustion systems such as internal combustion engines and gas turbine combustors [4], and building fires [5].

The underlying physics of flame–wall interactions in laminar flows as well as how flame extinction is induced and influenced by walls have been studied extensively in different aspects. As one of the most critical quantities for flame–wall interaction, the quenching distance was investigated theoretically and numerically with one-step global chemistry [6–8]. In addition, how the chemical kinetics (e.g., chaining-branching and radical recombination reactions) behaves during near-wall flame extinction was studied in terms of temperature dependence [9] and the radical kinetics [10,11]. The strong coupling between the wall and flame also leads to the flame bifurcations with respect to the varying parameters like wall temperature, equivalence ratio, and strain rate [12–14]. The effects of the laboratory scale burner geometries (e.g., curved and slit burners as well as perforated-plates) on the heat exchange and relevant flame dynamics (e.g., flash-back) were examined [15–17] and the correlations between wall temperature

and heat flux were also reported [18]. All the above studies contribute to understanding flame–wall interactions for laminar pre-mixed combustion with simplified flame configurations and/or chemical mechanisms. However, investigations for nonpremixed flames interacting with walls are quite few and, furthermore, the existence of turbulence in realistic burners renders the interactions more complicated: the turbulence can stretch the flame fronts and the flame can dampen the local turbulence [1], while the wall would modify the temporal and spatial turbulence scales near the wall [19]. Therefore, it is of practical significance to account for the turbulence effects on flame–wall interaction and the incurred flame extinction. This is of particular importance for burners where flames are anchored close to walls such as bluff-body stabilizers, which is the topic studied in this paper.

Concerning modeling the flame–wall interactions, the heat transfer between the turbulent flame and chamber wall has been studied in the large eddy simulation (LES) context. For instance, wall functions based on the temperature logarithmic law were used for predicting the wall heat fluxes [20,21]. However, the inclusion of wall heat loss into advanced combustion models is not straightforward due to the implementations needed to solve the energy equation. The enthalpy defect concept was first proposed by Bray and Peters [22] and used for defining the enthalpy deviation from the adiabatic profiles in mixture fraction space, caused by radiation and/or boundary heat loss. It was introduced into the flamelet model for wall heat loss by Hergart and Peters [23] and a similar approach was adopted by Song and Abraham [24] to improve the near-wall flame structure calculations in modeling of diesel combustion. The enthalpy defect approach was also adopted in conditional moment closure (CMC) modeling for a three-dimensional turbulent nonpremixed syngas flame with a cooling wall [25]. The additional source term representing the wall heat loss was included into the governing equations of conditional mean temperature in three-dimensional CMC method by

<sup>1</sup>Corresponding author.

Contributed by the Combustion and Fuels Committee of ASME for publication in the JOURNAL OF ENGINEERING FOR GAS TURBINES AND POWER. Manuscript received February 25, 2018; final manuscript received May 10, 2018; published online August 20, 2018. Assoc. Editor: Sunil Patil.

De Paola et al. [26] who simulated combustion in a direct-injection heavy duty diesel engine. The above were based on Reynolds-averaged Navier–Stokes and therefore could not analyze the unsteady heat transfer between the wall and flame and how the wall heat loss affects the transient flame dynamics. For flames stabilized by bluff-body stabilizers approaching blow-off, it has been shown by Kariuki et al. [27] that flame elements lie very close to the bluff body in a bluff body recirculating premixed flame, and similar observations were made by Cavaliere et al. [28] for nonpremixed flames close to extinction. The effects of the wall heat loss on the local extinction and lift-off of swirl nonpremixed flames close to the bluff body need to be examined and to be included in the simulation method. Recently, we incorporated the heat loss from chamber wall in simulating the blow-off transient in swirling flames [29]; however, focused analysis about the heat loss effects was not made there.

The goal of the current study is to apply LES with a three-dimensional CMC combustion subgrid model to a swirl-stabilized nonpremixed methane flame. The wall heat loss is modeled by introducing a source term in the conditionally filtered total enthalpy equation. The mathematical formulation, LES/3D-CMC, numerical implementations, and the information about the flow investigated are given in Secs. 2 and 3 presents the main results and discussion, followed by the conclusions in Sec. 4.

## 2 Mathematical Formulation and Flow Considered

**2.1 Large Eddy Simulation and Conditional Moment Closure Modelling.** The LES governing equations for mass, momentum, and mixture fraction are derived through Favre filtering their corresponding instantaneous equations. The constant Smagorinsky model by Fureby [30] is used to close the anisotropic part of the subgrid stress tensor  $\tilde{S}$  in the LES equations, i.e.,  $\tilde{S} - 2\tilde{\rho}kI/3 = -2\mu_t \mathbf{D}_{dev}$ . Here,  $\tilde{\rho}$  is the filtered density and  $k$  is the subgrid scale kinetic energy.  $\mathbf{I}$  is the identity tensor and  $\mathbf{D}_{dev}$  is the deviatoric part of the filtered strain rate tensor  $\tilde{\mathbf{D}}$ . The subgrid scale dynamic viscosity  $\mu_t$  is calculated as

$$\mu_t = c_k \Delta \tilde{\rho}^{k/2} \quad (1)$$

where  $\Delta$  is the filter width taken as the cube root of the LES cell volume  $V_{LES}$  and the constant  $c_k = 0.02$ . Based on the local equilibrium assumption, the algebraic relation is obtained for  $k$  as shown below:

$$\tilde{S} : \tilde{\mathbf{D}} + \tilde{\rho} \varepsilon = 0 \quad (2)$$

in which the symbol  $:$  denotes the double inner product of two tensors and the dissipation rate  $\varepsilon$  is modeled as  $\varepsilon = c_\varepsilon k^{3/2} / \Delta$  with  $c_\varepsilon = 1.048$ .

The filtered scalar dissipation rate  $\tilde{N}$  is calculated as [31]

$$\tilde{N} = \tilde{N}_{res} + \tilde{N}_{sgs} = \underbrace{D \nabla \tilde{\xi} \cdot \nabla \tilde{\xi}}_{resolved} + \underbrace{c_N \mu_t \tilde{\xi}'' / 2\tilde{\rho} \Delta^2}_{subgrid} \quad (3)$$

with  $\tilde{N}_{res}$  and  $\tilde{N}_{sgs}$  being the resolved and subgrid scalar dissipation, respectively. Their individual models have been formulated in Eq. (3).  $D$  denotes the mass diffusivity and is calculated through  $D = \mu / \tilde{\rho} Sc$  with Schmidt number  $Sc = 1$ .  $\mu$  is the molecular dynamic viscosity calculated through Sutherland's law. Here, the constant  $c_N = 42$  is used for the subgrid scalar dissipation model in Eq. (3), following calibration against measurements in jet flames [32].  $\tilde{\xi}$  and  $\tilde{\xi}''$  are the resolved mixture fraction and its subgrid variance. In the present investigation, the latter is modeled as [33]

$$\tilde{\xi}'' = c_v \Delta^2 \nabla \tilde{\xi} \cdot \nabla \tilde{\xi} \quad (4)$$

in which  $c_v = 0.1$ .

The conservative 3D-CMC equations for nonpremixed combustion are [25,34–38]

$$\underbrace{\partial Q_\alpha / \partial t}_{unsteady} + \underbrace{\nabla \cdot \tilde{\mathbf{U}} \tilde{\eta} Q_\alpha}_{convection} = \underbrace{Q_\alpha \nabla \cdot \tilde{\mathbf{U}} \tilde{\eta}}_{dilatation} + \underbrace{N \tilde{\eta} \partial^2 Q_\alpha / \partial \eta^2}_{micromixing} + \underbrace{\omega_\alpha \tilde{\eta}}_{chemistry} + \underbrace{e_f}_{turbulent diffusion} \quad (5)$$

where  $Q_\alpha = Y_\alpha | \tilde{\eta}$  is the conditionally filtered mass fractions of  $\alpha$ th species and  $\tilde{\eta}$  is the sample space variable for mixture fraction  $\xi$ .  $\tilde{\mathbf{U}} \tilde{\eta}$ ,  $N \tilde{\eta}$  and  $\omega_\alpha \tilde{\eta}$  are the conditionally filtered velocity, scalar dissipation rate, and reaction rates, respectively. The assumption  $\tilde{\mathbf{U}} \tilde{\eta} \approx \tilde{\mathbf{U}}$  is adopted here. The amplitude mapping closure model [39] is used for the conditionally filtered dissipation rate,  $N \tilde{\eta} = N_0 G(\eta)$ , where  $N_0$  and  $G(\eta)$  are  $N_0 = \tilde{N} / \int_0^1 \tilde{P}(\eta) G(\eta) d\eta$  and  $G(\eta) = \exp\left(-2[\text{erf}^{-1}(2\eta - 1)]^2\right)$ , respectively. The first-order CMC model is applied such that  $\omega_\alpha \tilde{\eta} = \omega_\alpha(Q_1, \dots, Q_n, Q_T)$  where  $n$  is the number of species and  $Q_T = T | \tilde{\eta}$  represents the conditionally filtered temperature.  $\tilde{P}(\eta)$  is the filtered probability density function (PDF) assumed to be beta-function shape and is calculated with  $\tilde{\xi}$  and  $\tilde{\xi}''$ . The turbulent subgrid diffusion term in Eq. (5) is  $e_f = -\nabla \cdot \left[ \frac{\tilde{\rho} \tilde{\eta} \tilde{P}(\eta) (\tilde{\mathbf{U}} \tilde{\eta} - \tilde{\mathbf{U}} | \tilde{\eta} Q_\alpha)}{\tilde{\rho} | \tilde{\eta} \tilde{P}(\eta)} \right]$  and modeled as  $e_f = \nabla \cdot (D_t \nabla Q_\alpha)$  [40].  $D_t$  is the turbulent subgrid diffusivity and modeled as  $D_t = \mu_t / \tilde{\rho} Sc_t$  with the turbulent Schmidt number  $Sc_t = 0.7$ .  $\tilde{\rho} | \tilde{\eta}$  is the filtered density.

The equation for the conditionally filtered total enthalpy  $Q_h = h | \tilde{\eta}$  has the same form as Eq. (5) excluding the chemistry term. To include the convective wall heat loss in the CMC model, the following term is introduced into the RHS of  $Q_h$  equation for CMC cells adjacent to a wall [23,26,29]

$$q_{w,\Omega} | \tilde{\eta} = -h(Q_T - T_w) \quad (6)$$

in which  $q_{w,\Omega} | \tilde{\eta}$  is the conditionally filtered volumetric heat loss and  $T_w$  is the wall temperature. The heat transfer coefficient  $h$  in Eq. (6) is predicted through  $h = \tilde{q}_{w,\Omega} / \tilde{\rho} | \tilde{\eta} \int_0^1 (Q_T - T_w) \tilde{P}(\eta) d\eta$ .  $\tilde{q}_{w,\Omega}$  (in units of  $\text{W/m}^3$ ) is the filtered volumetric heat loss, which is calculated through volume-averaging of the magnitude of the wall surface heat flux  $\tilde{q}_{w,S}$  (in units of  $\text{W/m}^2$ ) as  $\tilde{q}_{w,\Omega} = \int_{\partial\Omega} \tilde{q}_{w,S} dS / V_{LES}$  where  $\partial\Omega$  denotes the faces of the LES cell  $\Omega^{LES}$ . Here, the surface heat flux magnitude  $\tilde{q}_{w,S}$  is estimated from the LES as

$$\tilde{q}_{w,S} = -\tilde{q}_{w,S}^l - \tilde{q}_{w,S}^t = \lambda \nabla_n \tilde{T} + \lambda_t \nabla_n \tilde{T} \quad (7)$$

In Eq. (7),  $\tilde{T}$  is the filtered temperature. The gradient of the filtered temperature  $\nabla_n \tilde{T}$  is aligned with the wall normal direction.  $\tilde{q}_{w,S}^l$  and  $\tilde{q}_{w,S}^t$  denote the individual heat fluxes from laminar and turbulent heat transfer.  $\tilde{q}_{w,S}^t$  has been modeled using the classical Reynolds analogy in Eq. (7).  $\lambda = c_p \mu / Pr$  and  $\lambda_t = c_p \mu_t / Pr_t$  are the laminar and turbulent thermal conductivities, respectively, and  $c_p$  is the specific heat capacity at constant pressure. The molecular and turbulent Prandtl numbers are assumed to be  $Pr = 1$  and  $Pr_t = 0.7$ , respectively, over the entire flow field.

**2.2 Large Eddy Simulation/Conditional Moment Closure Data Coupling Strategy.** Considering the relatively small spatial variations of the conditional reactive scalars  $Q_\alpha$ , the CMC governing equations, i.e., Eq. (5), are solved on a coarse mesh different from the fine LES mesh [40,41]. In the present investigation, finite volume discretization is employed for both LES and CMC equations and the CMC cells are reconstructed based on the CMC nodes (red squares in Fig. 1) through selecting the CMC faces

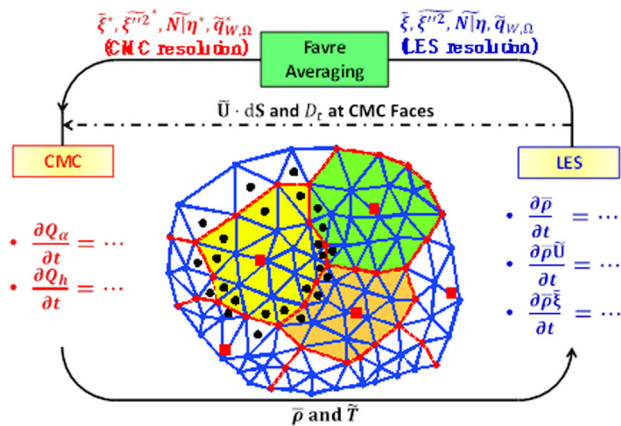


**Fig. 1 Schematic showing CMC cell reconstruction and coupling between LES and CMC solvers [29]. The two-dimensional mesh denotes the slice through a three-dimensional unstructured LES mesh. Lines enclosing the continuous grey cells are CMC edges while other lines are LES ones. Circles denote centroids of LES cells while squares CMC nodes. The cells enclosed by CMC edges are the reconstructed CMC cells.**

from the LES faces. This selection is based on the criterion that the owner and neighbor LES cells of one face must have different host CMC cells while the CMC boundary faces are directly duplicated from LES faces. For each LES cell, its host CMC cell is exclusive and identified based on the minimal distance between the LES cell centroids and CMC nodes. In turn, each CMC cell consists of a number of LES cells, which are highlighted in the same color in the mesh inset of Fig. 1, and for these LES cells, conditional reactive scalars  $Q_\alpha$  are uniform and obtained from their shared host CMC cell. It should be highlighted that the above strategy ensures the uniqueness of the whole reconstructed CMC meshes and the geometrical completeness of individual polyhedral CMC cells (see Fig. 1). No singleton LES cells would be left due to the mapping between the initially specified LES cells and CMC nodes.

The data coupling between the fine LES and coarse CMC meshes is illustrated in Fig. 1 as well. In particular, the conditionally filtered scalar dissipation rate for Eq. (5) in the CMC resolution,  $\widetilde{N|\eta^*}$ , is estimated through FDF-weighted integrating the conditional scalar dissipation,  $\widetilde{N|\eta}$ , over each LES cell constituting the host CMC cell

$$\widetilde{N|\eta^*} = \mathcal{L}_{\text{FDF}}(\widetilde{N|\eta}) \quad (8)$$

and the filtered volumetric heat loss in the CMC resolution for calculating  $h$  in Eq. (6) is obtained through

$$\widetilde{q}_{w,\Omega}^* = \mathcal{L}(\widetilde{q}_{w,\Omega}) \quad (9)$$

For the CMC cells,  $\widetilde{\xi}^*$  and  $\widetilde{\xi}^{n2*}$  are necessary to calculate the FDF. They are estimated as [40]

$$\widetilde{\xi}^* = \mathcal{L}(\widetilde{\xi}) \quad (10a)$$

$$\widetilde{\xi}^{n2*} = \mathcal{L}(\widetilde{\xi}^2) + \mathcal{L}(\widetilde{\xi}^{n2}) - \mathcal{L}^2(\widetilde{\xi}) \quad (10b)$$

In Eqs. (8)–(10),  $\mathcal{L}_{\text{FDF}}(x)$  and  $\mathcal{L}(x)$  are formulated as

$$\mathcal{L}_{\text{FDF}}(x) = \int_{\Omega^{\text{CMC}}} \bar{\rho} \widetilde{P}(\eta) x d\Omega / \int_{\Omega^{\text{CMC}}} \bar{\rho} \widetilde{P}(\eta) d\Omega \quad (11a)$$

$$\mathcal{L}(x) = \int_{\Omega^{\text{CMC}}} \bar{\rho} x d\Omega / \int_{\Omega^{\text{CMC}}} \bar{\rho} d\Omega \quad (11b)$$

denoting the FDF-weighted Favre averaging and Favre averaging operators, respectively.

In addition, as shown in Fig. 1, the volume fluxes  $\widetilde{U} \cdot dS$  ( $S$  is the CMC face normal vectors) and turbulent diffusivity  $D_t$  at the CMC faces are interpolated based on the flow and turbulence properties at their neighboring and owner LES cells.  $\widetilde{U} \cdot dS$  and  $D_t$  should be provided from LES solver to the CMC solver for the flux calculations of convection and turbulent diffusion terms in Eq. (5). Emphasis should be laid here that the interpolations and flux predictions in discretizing Eq. (5) should be performed based on the LES cell centroids (black circles in Fig. 1) instead of CMC nodes since the latter are not necessarily the geometrical centroids in the present implementations. In this sense, the topology (e.g., mesh nonorthogonality and skewness) of reconstructed CMC cells would not constitute the mesh-induced error source when discretizing Eq. (5). Instead, the flux conservation for the CMC cells can be ensured here since the current strategy does not introduce any kind of averaging for  $\widetilde{U}$  and therefore  $\widetilde{U}|\eta$ , which is of great importance in accurately predicting the transport between CMC cells in physical space. In addition, the local refinement of CMC nodes would be beneficial in capturing the large spatial variations of  $Q_\alpha$ , e.g., near the bluff body and chamber walls. In principle, the approach used in Ref. [25] for flux prediction (i.e., directly discretizing the terms of convection, dilatation, and diffusion on the faces from the original meshes using these nodes as the centroids) can also be applied here but the potential inaccuracy in terms of flux conservation and mass inconsistency would be introduced.

The unconditionally filtered quantities  $\widetilde{f}$  (including  $\bar{\rho}$ ,  $\bar{T}$  and other scalars) at the LES resolution are obtained through  $\widetilde{f} = \int_0^1 \widetilde{f|\eta^*} \widetilde{P}(\eta) d\eta$ .  $\widetilde{f|\eta^*}$  is the conditionally filtered scalars (e.g.,  $\bar{\rho}|\eta^{-1}$ ,  $Q_T$  and  $Q_\alpha$ ) provided by the corresponding host CMC cells.

### 2.3 Flow Considered and Numerical Implementations.

Figure 2 is a schematic of the burner studied experimentally at the University of Cambridge [28]. A bluff body (see Fig. 2(b)) with diameter  $D_b = 0.025$  m is fitted concentrically in a pipe with  $D_p = 0.037$  m. The fuel injector lies at the center of bluff body top with diameter  $D_f = 0.004$  m. The size of the rectangular chamber is  $0.095 \times 0.095 \times 0.15$  m<sup>3</sup>. The air bulk velocity  $U_{a,b}$  at the annular pipe outlet is 19.1 m/s while that of the nonswirling pure methane jet  $U_{f,b}$  is 29.2 m/s. The temperature for both gases is 294 K. The swirl number  $S_N$  is 1.23 following Beer and Chigier's formula [42], i.e.,

$$S_N = \frac{2}{3} \frac{1 - (D_{\text{hub}}/D_p)^3}{1 - (D_{\text{hub}}/D_p)^2} \tan\theta \quad (12)$$

Here,  $D_{\text{hub}} = 0.011$  m is the swirler hub diameter and  $\theta = 60$  deg is the swirler vane angle with respect to the streamwise direction. The Reynolds number for the air stream based on the annular opening, i.e.,  $D_p - D_b$ , and  $U_{a,b}$  is about 17,700, while that for fuel jet based on  $D_f$  and  $U_{f,b}$  is about 4500. The stoichiometric mixture fraction is  $\xi_{\text{st}} = 0.055$ .

Mixture fraction space is discretized by 51 nodes clustered around  $\xi_{\text{st}}$ . In physical space, the Cartesian coordinate origin lies at the center of the circular fuel injector and  $x$  is the streamwise direction.  $y$  and  $z$  are normal to the side chamber walls. The LES domain includes the swirler, annulus, chamber, and a downstream hemisphere far field (not shown in Fig. 2) while the CMC domain consists of a partial annulus (without swirler) starting 0.02 m upstream of bluff body top, combustor and far field. Around 10 million tetrahedral LES cells (see the distribution in Fig. 3) are used while the number of the reconstructed polyhedral CMC cells is about 140,000. Within the flame region ( $0 < x/D_b < 2.4$ ), the distribution of the number of LES cells contained by one CMC cell is plotted in Fig. 4(a). The mean of LES cells for one CMC

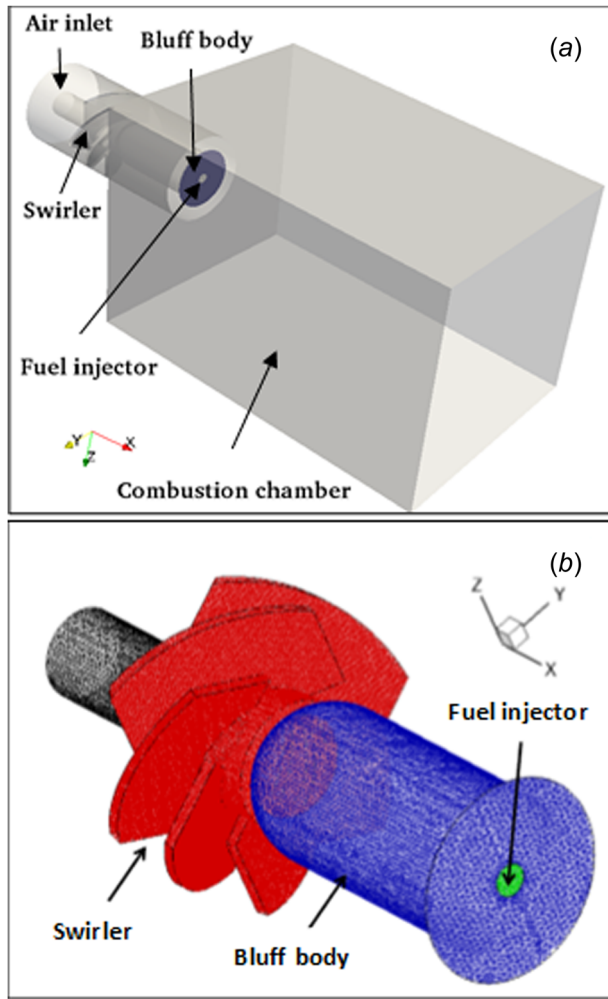


Fig. 2 (a) Schematic of the burner and (b) the swirler as well as the bluff body

cell is about 95. Figure 4(b) presents the number of CMC faces constituting one CMC cell. The number of the CMC faces is about 4,800,000 accounting for 23% of the LES faces and is roughly 16.5 times the face number (about 300,000) when these CMC nodes are used as cell centroids for generating purely tetrahedral cells. The mean of the CMC face number per CMC cell is 66.

For CMC boundaries in  $\eta$ -space, air and fuel with temperature 294 K are specified at  $\eta = 0$  and  $\eta = 1$ , respectively. All the CMC cells are initialized by the fully reactive 0D-CMC solutions (here, 0D-CMC calculations refer to solving Eq. (5) only with unsteady, micromixing, and chemistry terms, with a prescribed constant scalar dissipation) with an intermediate value for the peak scalar dissipation  $N_0 = 50$  1/s. Inert mixing solutions in  $\eta$ -space are injected into fuel and air inlets. For the wall boundaries in the CMC domain, inert mixing solutions are specified, implying full quenching at the wall is being assumed.

For the LES boundary conditions, at all inlets, zero pressure gradient conditions are applied. For velocity and mixture fraction, Dirichlet conditions are enforced. Random noise with 5% intensity is imposed for the velocities at both air and fuel inlets. The total pressure is fixed to be atmospheric at the far-field outlet. No slip condition for velocity and zero gradient for mixture fraction are enforced at the walls. Also, the walls are assumed to be chemically inert and cold ( $T_w = 298$  K). It should be emphasized that the assumed wall temperature is below the typical wall temperature values for most hydrocarbon combustion devices, which might be in the region 400–600 K [1]. However, it is expected that this would not qualitatively affect the conclusions in the

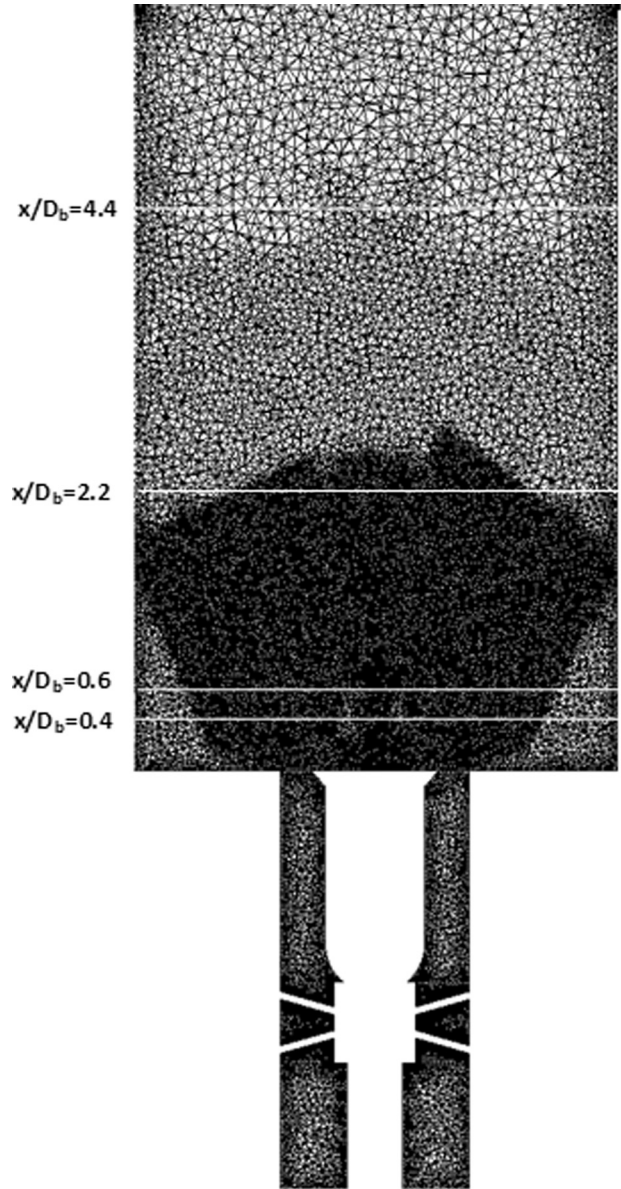


Fig. 3 Schematic of LES mesh distribution in the annulus and combustion chamber

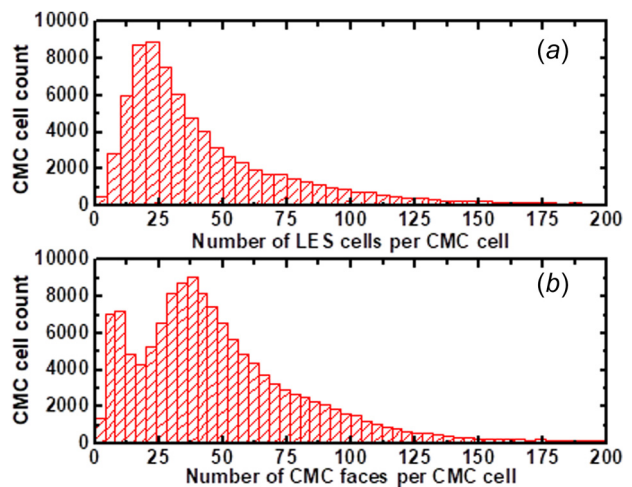


Fig. 4 Reconstructed CMC mesh statistics: number of (a) LES cells and (b) CMC faces constituting one CMC cell

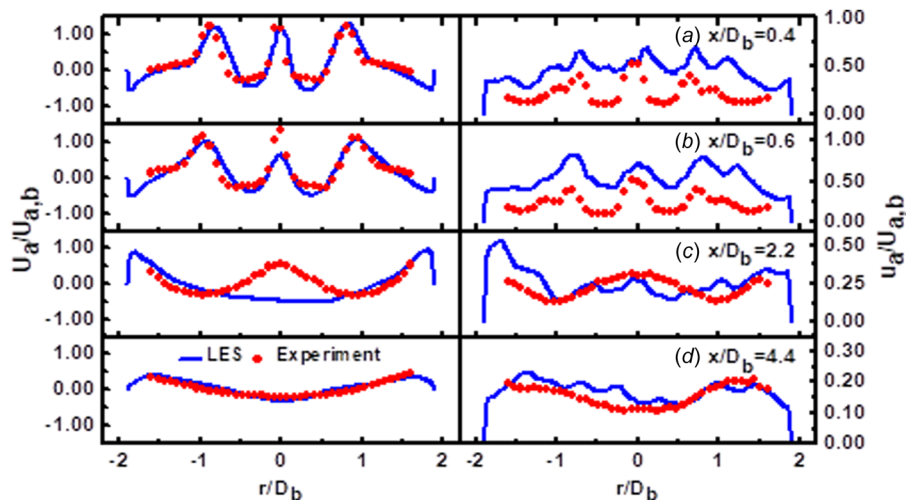


Fig. 5 Radial profiles of mean (left) and rms (right) axial velocity at  $x/D_b = 0.4, 0.6, 2.2$  and  $4.4$ . These locations are indicated in Fig. 3.

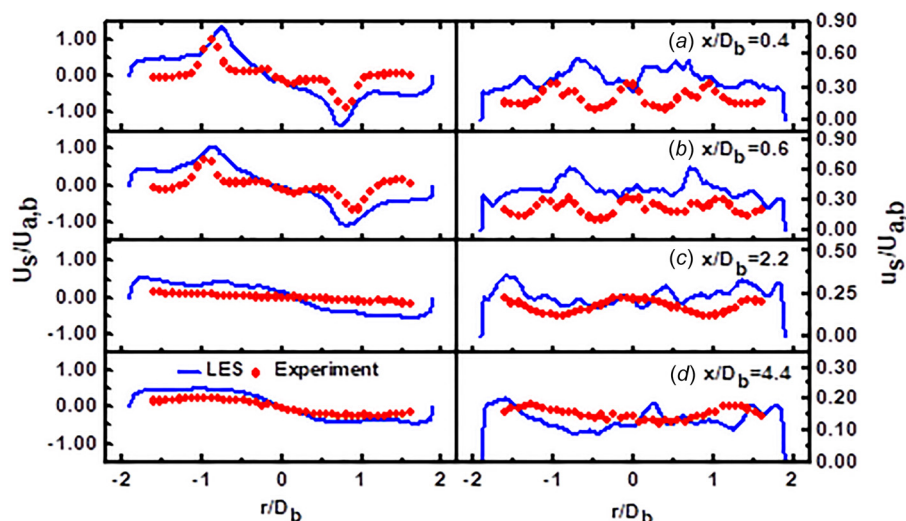


Fig. 6 Radial profiles of mean (left) and rms (right) swirl velocity at  $x/D_b = 0.4, 0.6, 2.2$  and  $4.4$ . These locations are indicated in Fig. 3.

present paper.  $y^+ < 4$  for near-wall LES mesh is basically satisfied to accurately predict the near-wall temperature gradient. In this paper, only the bluff body wall heat loss effects are investigated, which are more relevant to the lift-off and local extinction. The instantaneous flow and mixing fields are initialized by the results from an LES where the conditional profiles of reactive scalars are from a steady 0D-CMC calculation.

The LES and CMC governing equations are solved by OPENFOAM and in-house codes, respectively. The time-step for both solvers is  $\Delta t = 1.5 \times 10^{-6}$  s. Low Ma number assumption is applied in LES. The PISO algorithm is used for the velocity–pressure coupling and a second-order implicit Crank–Nicholson scheme for time marching. In the CMC solver, the convection term is discretized with first-order upwind scheme while the modeled turbulent diffusion term with second-order central differencing. The conditional dilatation term in Eq. (5) is discretized as a source term here. Full operator splitting strategy is employed for solving Eq. (5) and the conditional chemical source term  $\omega_x|\eta$  is solved with VODPK [43]. The ARM2 mechanism by Sung et al. [44] is used for the methane/air combustion. The simulations were run on 80 2.53 GHz Xeon CPUs with 3 GB RAM for

each processor and around 24 h were needed for 0.001 s of physical time.

### 3 Results and Discussion

**3.1 Velocity Statistics.** The axial and swirl velocity statistics at four streamwise positions are compared with the corresponding experimental results [45] in Figs. 5 and 6 and the mean and rms from the simulations reasonably reproduces the main features of the flow (e.g., confined corner and long inner recirculation zones, i.e., CRZ and IRZ, as well as the solid-body rotating regions within  $-0.8 \leq r/D_b \leq 0.8$  and  $x/D_b < 1$  shown in Fig. 6). However, the fuel jet penetration is underpredicted in the LES, which can be observed by the underprediction of the central mean axial velocity at  $x/D_b = 0.6$  and  $2.2$  in Fig. 5. This may be caused by the fact that the streamwise adverse pressure gradients along the centerline are overestimated, which is related to the overprediction of mean swirl velocities at  $x/D_b = 0.4$  and  $0.6$  shown in Fig. 6. In addition, the rms of both axial and swirl velocities at  $x/D_b = 0.4$  and  $0.6$  from the LES is overpredicted. The higher rms quantities in LES may be affected by the overprediction of the turbulence

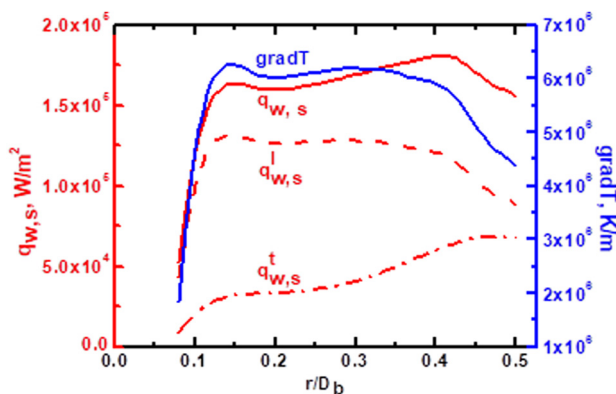
near the annulus exit. Generally, the statistics of axial and swirl velocities from the simulation show reasonable agreement with the experimental results.

**3.2 Wall Heat Flux and Local Extinction.** Figure 7 shows radial profiles of the mean heat flux  $q_{w,S}$  and the temperature gradient on the bluff body surface, i.e.,  $0.08 \leq r/D_b \leq 0.5$ . Here, the averaging is performed both in time and in the azimuthal direction. As the radius increases, the mean wall surface heat flux  $q_{w,S}$  and temperature gradient sharply increase at  $0 \leq r/D_b < 0.15$  and reach their individual plateaus at  $r/D_b = 0.15$ , and eventually decrease at  $r/D_b > 0.4$ . Clearly, the high values on the middle section of the surface ( $0.15 < r/D_b < 0.4$ ) are attributed to the contact between the cold surface and the flames as well as recirculating hot gases in IRZ while the relatively low heat fluxes at low and large radii result from the cold streams of air and fuel jets.

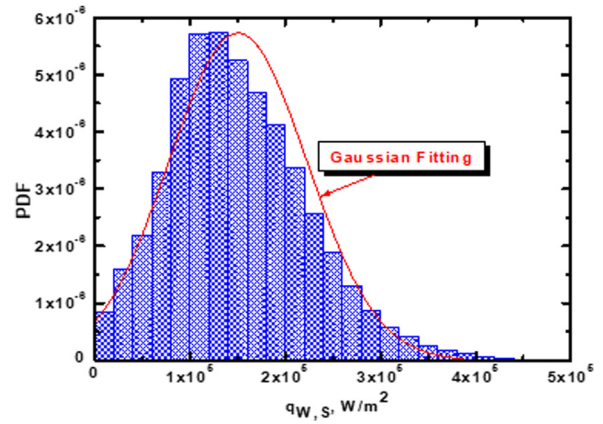
Figure 7 also presents radial distributions of the mean laminar and turbulent heat fluxes, i.e.,  $q_{w,S^l}$  and  $q_{w,S^t}$ .  $q_{w,S^l}$  is much lower than  $q_{w,S^t}$  on the whole surface and the fraction of the mean turbulent heat flux,  $q_{w,S^t}/q_{w,S}$ , monotonically increases from about 15% at  $r/D_b = 0.08$  to about 45% at  $r/D_b = 0.5$ . The laminar heat flux  $q_{w,S^l}$  basically follows the temperature gradient variations while, interestingly,  $q_{w,S^t}$  increases monotonically with the radius. Clearly, the turbulent heat flux  $q_{w,S^t}$  is directly linked to the turbulent viscosity  $\mu_t$  shown in Eq. (7) and therefore to the subgrid kinetic energy  $k$  shown in Eq. (1). Since the velocity rms close to bluff body (e.g.,  $x/D_b = 0.4$  in Figs. 5(a) and 6(a)) is over-predicted, it should be acknowledged that  $q_{w,S^t}$  close to  $r/D_b = 0.5$  is accordingly over-predicted.

Figure 8 demonstrates the probability density function (PDF) of the instantaneous bluff body surface wall fluxes  $\tilde{q}_{w,S}$  based on the whole surface at all simulated time instants. The PDF is close to a Gaussian distribution, although clipped at zero, implying that cold air and fuel streams are occasionally present at the wall. This feature is different from the results reported in Wang and Trouvé [46] with two-dimensional direct numerical simulation of ethylene/air nonpremixed flames near a wall, where the PDF of wall heat fluxes is quite narrow and very few samples can be seen near zero. This discrepancy can be attributed to the existence of the cold air and fuel inlets near the bluff body and also the recirculating fresh gas from downstream in IRZ. Furthermore, the mean and peak heat fluxes in Fig. 8 are approximately  $1.5 \times 10^5$  and  $5 \times 10^5$  W/m<sup>2</sup>, respectively. They show good agreement with the heat flux estimation in Lataillade et al. [47] where the order of magnitude of  $5 \times 10^5$  W/m<sup>2</sup> was obtained from methane/air flames at 1 bar pressure and 300 K wall temperature.

Figure 9 shows the variations of the conditionally filtered volumetric heat loss  $q_{w,\Omega}|\eta$  and total enthalpy  $Q_h$  from one CMC cell near the bluff body. Each curve is from one instant and in Fig. 9(a) large fluctuations of  $q_{w,\Omega}|\eta$  can be seen with respect to



**Fig. 7** Radial profiles of mean heat flux and temperature gradient on the bluff body surface ( $0.08 \leq r/D_b \leq 0.5$ )



**Fig. 8** Probability density function of the bluff body surface heat flux. The data are extracted both in time and space over the whole bluff body surface.

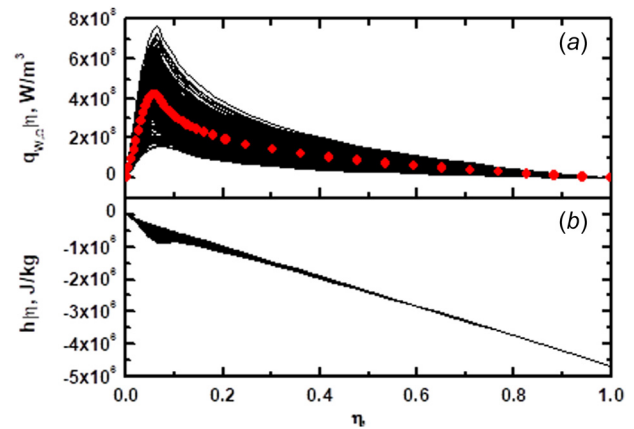


**Fig. 9** Variations of conditionally filtered (a) volumetric heat loss and (b) total enthalpy. Symbols: mean conditional heat flux. The data are from a CMC cell immediately adjacent to the bluff body surface (CMC cell centroid coordinate:  $x/D_b = 0.012$ ,  $y/D_b = 0.4$  and  $z/D_b = 0$ ).

its mean profile (denoted as the symbols) in the whole mixture fraction space. The introduction of the volumetric heat loss into the conditionally filtered total enthalpy equations makes  $Q_h$  deviate from the adiabatic profiles, which is a straight line between  $\eta = 0$  and  $\eta = 1$ . The considerable fluctuations of  $Q_h$  occur at about  $\eta = \xi_{st}$  resulting from the large fluctuations of  $q_{w,\Omega}|\eta$  there as shown in Fig. 9(a).

The time records of some important conditionally filtered scalars, scalar dissipation rate, and volumetric heat loss at  $\eta = \xi_{st}$  are presented in Fig. 10. Between  $t = 0.04$  s and 0.04125 s, the flame is burning based on the values of  $q|\xi_{st}$ ,  $Y_{OH}|\xi_{st}$  and  $T|\xi_{st}$  shown in Figs. 10(a)–11(c). However, at around  $t = 0.04125$  s, the flame is quenched (low  $q|\xi_{st}$ ,  $Y_{OH}|\xi_{st}$  and  $T|\xi_{st}$ ) due to the large scalar dissipation as shown in Fig. 10(d). The extinction continues until  $t = 0.043$  s when the stoichiometric scalar dissipation  $N|\xi_{st}$  becomes very low and the re-ignition occurs. Based on Fig. 10(e) and similar results from other near-wall CMC cells,  $q_{w,\Omega}|\xi_{st}$  basically follows the evolutions of  $T|\xi_{st}$  but with some high-frequency oscillations. It also shows the pronounced decrease/increase during the onsets of extinction/re-ignition. This can be expected to facilitate the occurrence of these two critical flame behaviors based on the present results.

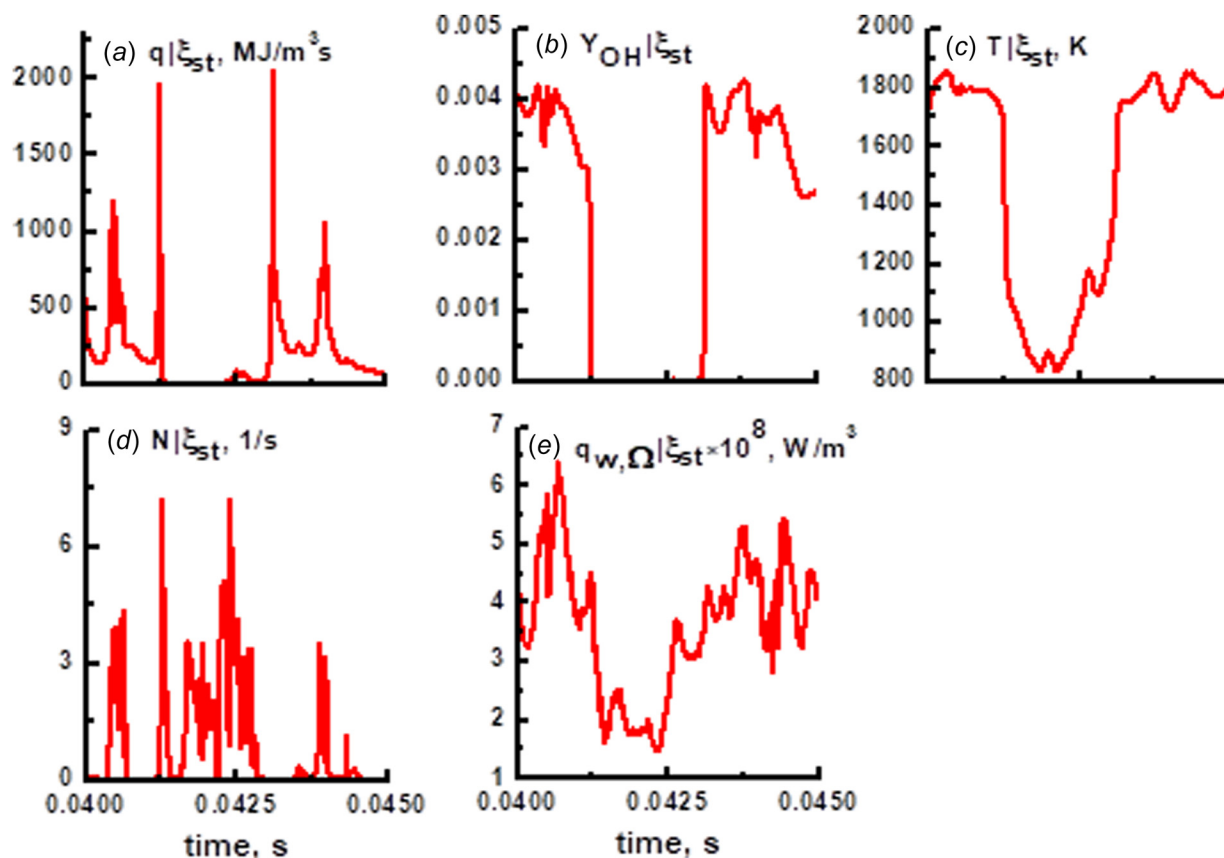


Fig. 10 Time records of conditionally filtered (a) heat release rate, (b) OH mass fraction, (c) temperature, (d) scalar dissipation, and (e) volumetric heat loss at  $\eta = \zeta_{st}$  from the same CMC cell as in Fig. 9

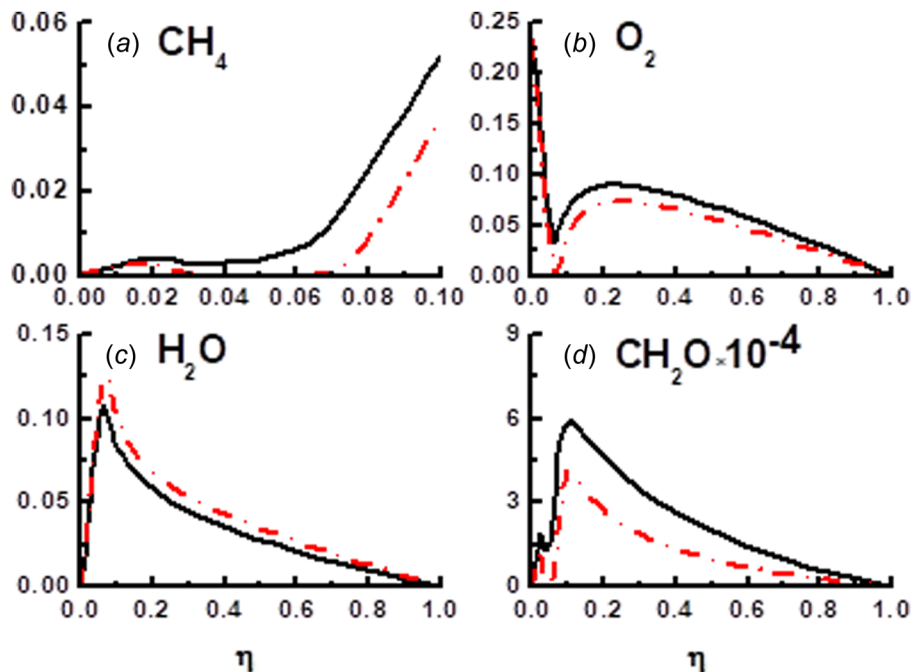


Fig. 11 Comparisons of the mean conditional mass fractions of (a)  $\text{CH}_4$ , (b)  $\text{O}_2$ , (c)  $\text{H}_2\text{O}$ , and (d)  $\text{CH}_2\text{O} \times 10^{-4}$  between adiabatic (dash-dot lines) and heat loss (solid lines) cases. The same CMC cell as in Fig. 9.

**3.3 Near-Wall Conditional Flame Structures.** To investigate the wall heat loss effects, LES/3D-CMC simulation with adiabatic wall conditions (termed as adiabatic case hereafter) was also conducted in which all the other numerical implementations

were exactly the same as those of the present case (termed as heat loss case hereafter). The statistics about the velocities and local extinction from the adiabatic case have been discussed by Zhang et al. [34].

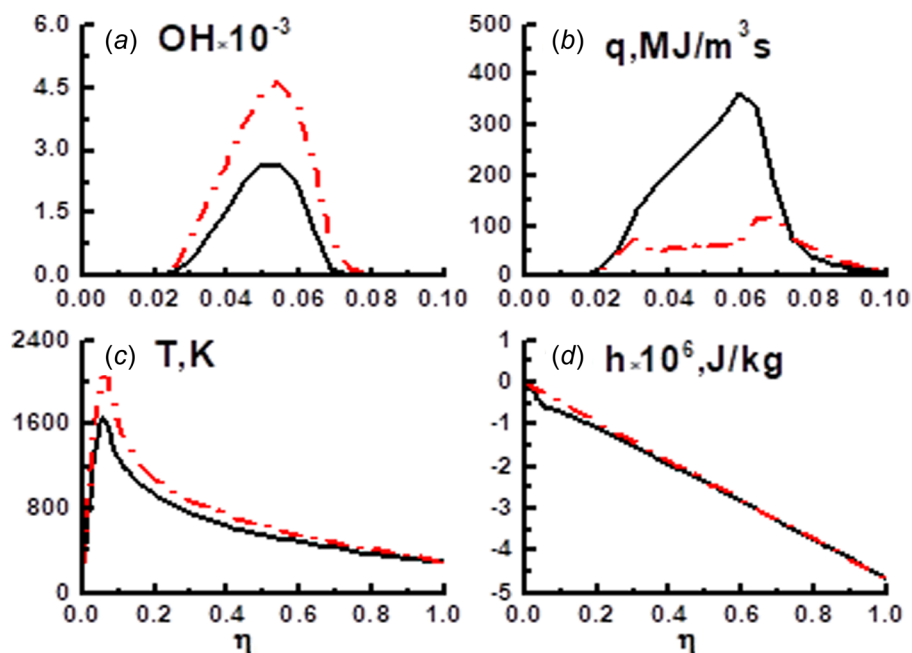


Fig. 12 Comparisons of the mean conditional (a) OH mass fraction, (b) heat release rate, (c) temperature, and (d) total enthalpy between adiabatic (dash-dot lines) and heat loss (solid lines) cases. The same CMC cell as in Fig. 9.

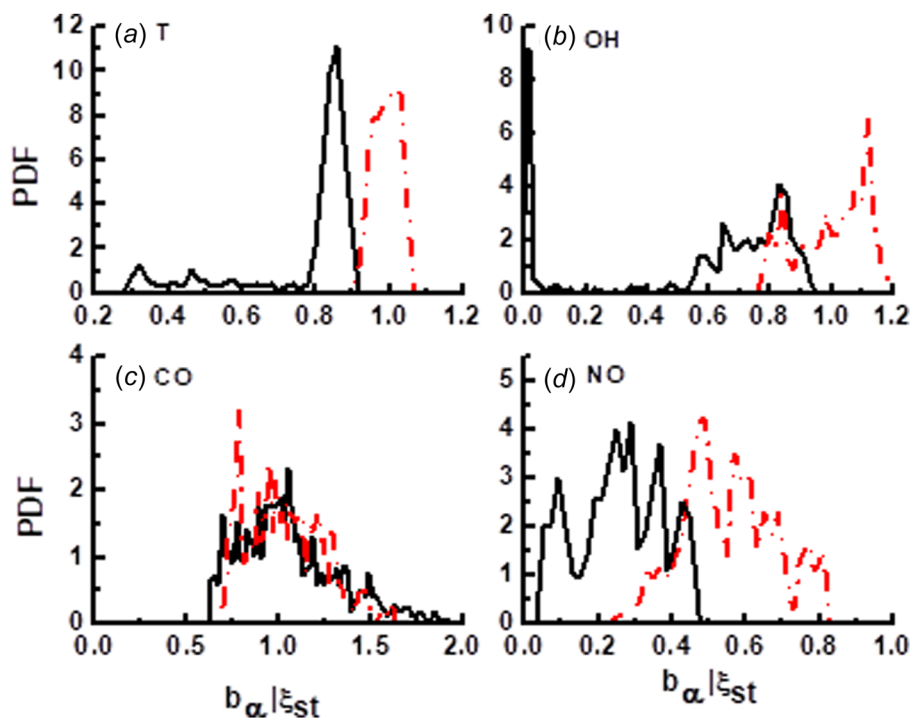
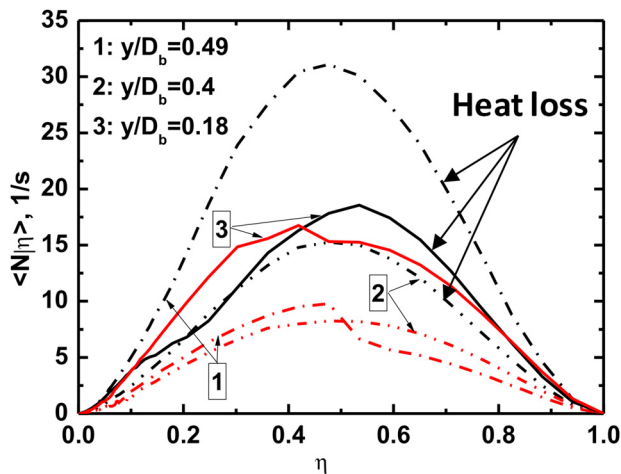


Fig. 13 Probability density function of reactedness at  $\eta = \xi_{st}$  from (a) temperature, mass fractions of (b) OH, (c) CO, and (d) NO. Dash-dot lines: adiabatic case, solid lines: heat loss case.

Figures 11 and 12 show the comparisons of mean flame structures in mixture fraction space predicted from heat loss and adiabatic cases. These results are extracted from the same CMC cell as that in Fig. 9. The mean conditional mass fractions of reactants (i.e.,  $\text{CH}_4$  and  $\text{O}_2$  in Figs. 11(a) and 11(b))/products (e.g.,  $\text{H}_2\text{O}$  in Fig. 11(c)) are higher/lower in the heat loss case than those in the adiabatic simulation, indicating incomplete reactions when wall heat loss is included. The conditional mass fraction of  $\text{CH}_2\text{O}$  in

Fig. 11(d) is higher in the heat loss case. The mean profiles of OH mass fraction in  $\eta$ -space, heat release rate and temperature are shown in Figs. 12(a)–12(c). Compared to the adiabatic results,  $\overline{Y_{\text{OH}}|\eta}$  and  $\overline{T|\eta}$  in the heat loss case are obviously lower and, conversely,  $\overline{q|\eta}$  is much higher within  $0.025 < \eta < 0.075$ . In addition, the inclusion of wall heat loss term in Eq. (6) leads to a considerable enthalpy defect around  $\eta = \xi_{st}$  as shown in Fig. 12(d).



**Fig. 14** The mean conditional scalar dissipation rates of three near-wall CMC cells ( $x/D_b = z/D_b = 0$ ) from adiabatic and heat loss cases

The conditional reactedness [48],  $\widetilde{b_x|\eta}$ , is calculated in the CMC cell investigated in Figs. 11 and 12 through

$$\widetilde{b_x|\eta} = \left( \widetilde{Y_{x,b}|\eta} - Y_{x,m}|\eta \right) / \left( \widetilde{Y_{x,b}|\eta} - Y_{x,m}|\eta \right) \quad (13)$$

In Eq. (13),  $Y_{x,b}|\eta$  and  $Y_{x,m}|\eta$  are the fully burning 0D-CMC solutions with  $N_0 = 5$  1/s and inert mixing ones, respectively. The extinction solutions are indicated by  $\widetilde{b_x|\eta} = 0$  while the fully burning profiles are reached when  $\widetilde{b_x|\eta}$  is close to or larger than unity. Figure 12 presents the PDF of reactedness at  $\eta = \xi_{st}$ ,  $\widetilde{b_x|\xi_{st}}$ , from temperature and mass fractions of OH, CO and NO from the heat loss and adiabatic cases. Clearly, in both cases,  $b_{OH}|\xi_{st}$  and  $b_T|\xi_{st}$  in Figs. 13(a) and 13(b) show the peaks when they are close to unity. However, in the heat loss case, the peaks of  $b_{OH}|\xi_{st}$  and

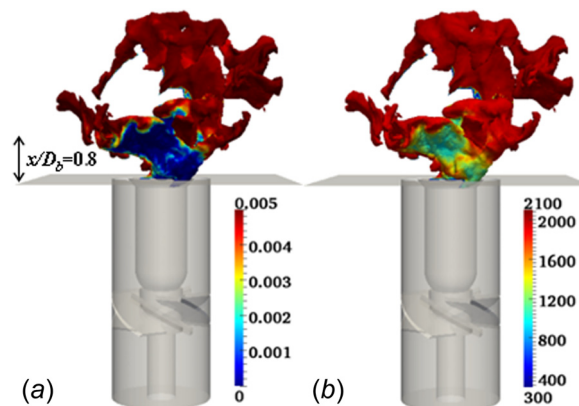


**Fig. 16** Iso-surfaces of instantaneous stoichiometric mixture fraction colored by conditional (a) OH mass fraction and (b) temperature at stoichiometry

$b_T|\xi_{st}$  are shifted toward smaller values, which imply weakened reactivity. For  $b_{OH}|\xi_{st}$ , another peak appears approaching zero, indicating the instantaneous extinction at the present CMC cell when wall heat loss is considered. However, for  $b_{CO}|\xi_{st}$  and  $b_{NO}|\xi_{st}$  in both cases, the distributions are wide. The PDF of  $b_{CO}|\xi_{st}$  is negligibly affected by the heat loss while that of  $b_{NO}|\xi_{st}$  move toward smaller values when wall heat loss is included. The results in Figs. 11–13 only correspond to one selected CMC cell but similar findings can also be obtained from other near-wall CMC cells.

The mean conditional scalar dissipation rates  $\langle N|\eta \rangle$  from the adiabatic and heat loss cases are compared in Fig. 14. For all three CMC cells corresponding to different radial positions (i.e.,  $y/D_b = 0.18, 0.4$ , and  $0.49$ ), adjacent to the bluff body,  $\langle N|\eta \rangle$  in the heat loss case is always larger than that in adiabatic one. This difference concerning  $\langle N|\eta \rangle$  explains the comparisons of mean flame structures in Figs. 11 and 12. Also, the difference of  $\langle N|\eta \rangle$  between two cases increases with the increased  $y/D_b$ . This implies that the wall heat loss greatly influences scalar dissipation near the outer part (with relatively large radii) of the bluff body

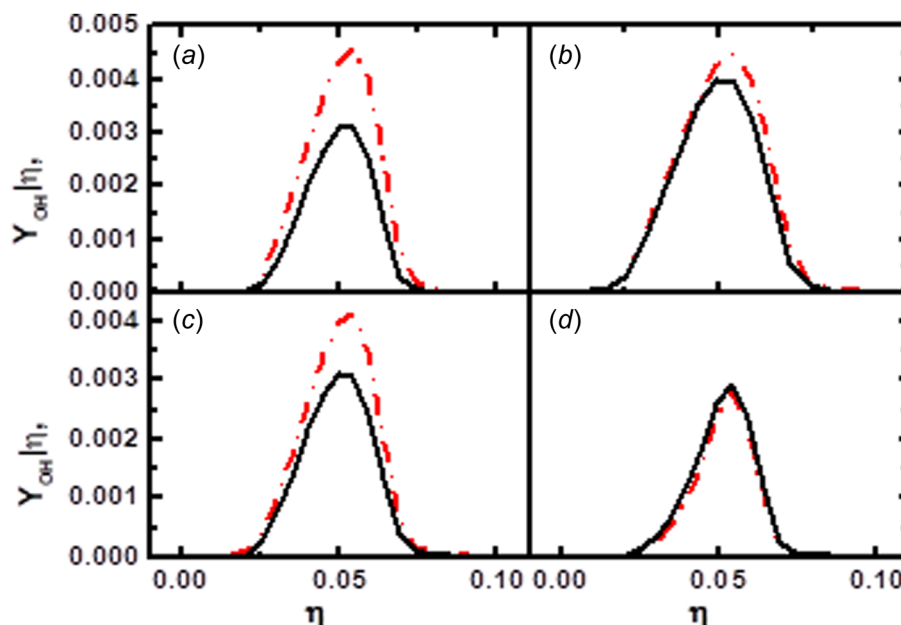


**Fig. 15** Comparisons of mean conditional OH mass fractions between adiabatic (dash-dot lines) and heat loss (solid lines) cases at four streamwise positions  $x/D_b =$  (a) 0.03, (b) 0.17, (c) 0.8, and (d) 1.6 with  $y/D_b = 0.4$  and  $z/D_b = 0$

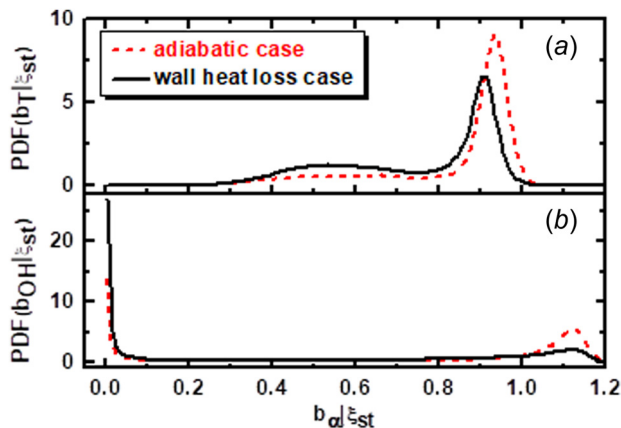


Fig. 17 Probability density function of reactedness at  $\eta = \xi_{st}$  from (a) temperature and (b) OH mass fraction corresponding to the three-dimensional stoichiometric iso-surface within  $0 \leq x/D_b \leq 0.8$

surface, where the iso-surfaces of instantaneous  $\xi_{st}$  and the flame base are occasionally attached to. However, the peak values of  $\langle N|\eta \rangle$  in these three CMC cells are still well below the critical peak value from 0D-CMC calculations ( $N_0 \approx 170$  1/s). This is consistent with the previous finding [32,34] that in LES/CMC the emergence of local extinction is not a simple function of the local and instantaneous scalar dissipation, but also a result of physical transport.

**3.4 Lift-Off.** The streamwise variations of the mean conditional mass fraction of OH,  $\langle Y_{OH}|\eta \rangle$ , are shown in Fig. 15 through comparing the heat loss and adiabatic results. It can be observed that  $\langle Y_{OH}|\eta \rangle$  in the adiabatic case is higher than in the heat loss case but the difference becomes negligible at  $x/D_b = 1.6$ . Iso-surfaces of instantaneous mixture fraction  $\xi_{st}$  colored by  $Y_{OH}|_{\xi_{st}}$  and  $T|_{\xi_{st}}$  (from the host CMC cells of the local LES meshes) in

the heat loss case are plotted in Fig. 15. At the iso-surfaces close to the bluff body, large flame holes quantified by low  $Y_{OH}|_{\xi_{st}}$  ( $< 0.001$ ) and  $T|_{\xi_{st}}$  ( $< 1200$  K) can be observed. This explicitly manifests the instantaneous extinction in  $\eta$ -space at the flame base regardless of the local mixing state, which can also be observed in the experiment [28].

The localized extinction close to the bluff body surface indicated in Fig. 16 is also seen in the adiabatic case as discussed by Zhang et al. [34] where it is attributed to the strong convection approaching the swirling air inlet. To appreciate how the wall heat loss affects the flame reactivity close to the bluff body, Fig. 17 presents the PDFs of reactedness at stoichiometry from temperature and OH mass fraction, i.e.,  $b_T|_{\xi_{st}}$  and  $b_{OH}|_{\xi_{st}}$ . Here, the samples include 50 time instants and each instant is extracted from about 3000 CMC cells enclosing the three-dimensional iso-surfaces of the instantaneous stoichiometric mixture fraction near the bluff body, i.e.,  $0 \leq x/D_b \leq 0.8$  (marked in Fig. 16(a)). In the adiabatic case,  $b_T|_{\xi_{st}}$  has a single peak which is centered at 0.92 with some negative skewness, indicating some degree of instantaneous extinction at the flame base. The extinction is also characterized by the pronounced bimodality in PDF of  $b_{OH}|_{\xi_{st}}$  in Fig. 17(b). In the heat loss case, the negative skewness of the PDF of  $b_T|_{\xi_{st}}$  is intensified and the PDF of  $b_{OH}|_{\xi_{st}}$  tends to have a single peak around zero. Both features concerning  $b_T|_{\xi_{st}}$  and  $b_{OH}|_{\xi_{st}}$  statistically indicate the weakened reactivity in the local CMC cells at the flame base when the bluff body heat loss effects are taken into account.

The PDF of the lift-off height  $h_L$  extracted from the  $xoy$  plane is presented in Fig. 18(a). Similarly to the definition in the experiment [28] and previous LES/3D-CMC simulations considering wall heat loss [34],  $h_L$  is the streamwise distance between the bluff body surface to the position along the  $\xi_{st}$  iso-line where  $Y_{OH}$  is critically larger the 0D-CMC threshold (i.e., 0.00024). 200 samples are extracted equally from both left and right flame branches close to the bluff body edge and 188 samples of those showed lifted flame. Only the snapshots with  $h_L > 0.5$  mm are considered here for calculating the PDF of  $h_L$ . The counterpart results from

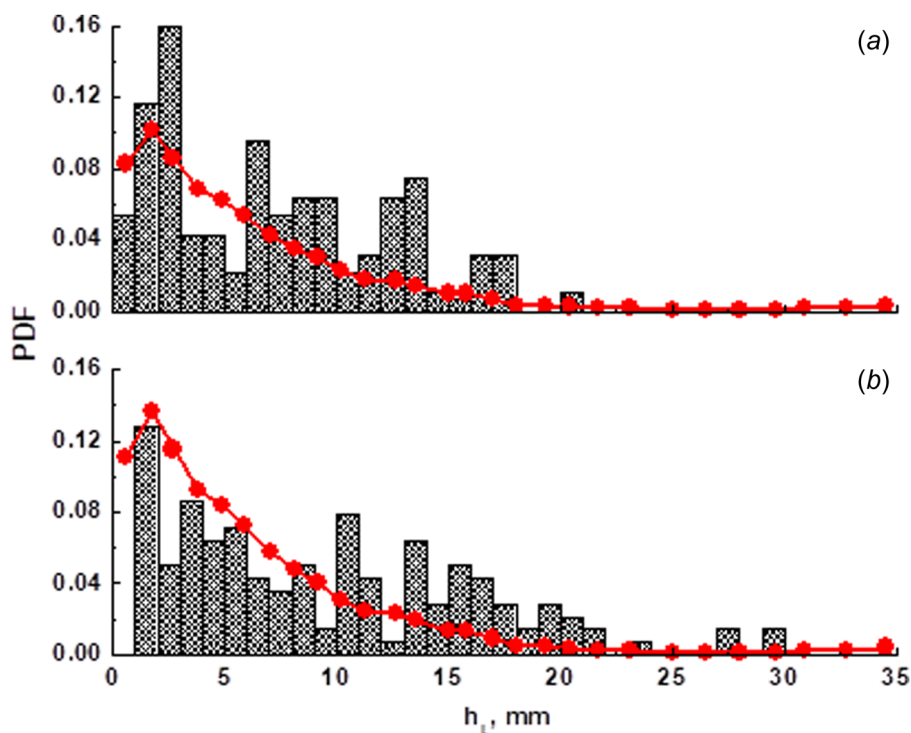


Fig. 18 Probability density functions of lift-off height from simulations with (a) heat loss and (b) adiabatic walls [34]. Line: experimental results [28].

the simulations with adiabatic bluff body [34] are also given in Fig. 18(b) for comparison. From Fig. 18(a), it can be seen that the PDF of  $h_L$  from the simulation agrees reasonably with the measured results. However, an overprediction around  $h_L = 3$  mm and  $7 \text{ mm} < h_L < 14$  mm exist and actually the overprediction of  $h_L$  is also observable for the range  $10 \text{ mm} < h_L < 20$  mm as shown in Fig. 18(b). In general, the influence of wall heat loss on the PDF of lift-off height  $h_L$  is relatively small, which implies that although heat losses reduces reactivity, the flame stabilization mechanism is a stronger function of the aerodynamic straining than the heat loss to the bluff body. This is broadly consistent with the measurements in Ref. [49] where the leanest equivalence ratio for blow-off in a premixed flame stabilized on a metal bluff body was smaller by only about 10% compared to the blow-off condition with a ceramic bluff body.

## 4 Conclusions

Large eddy simulation with three-dimensional conditional moment closure combustion model is applied to a swirling non-premixed methane flame with local extinction. The convective wall heat loss is included as a source term in the conditionally filtered total enthalpy equation for the CMC cells adjacent to walls. The mean heat flux is high on the middle bluff body surface but low near its edges. The turbulent heat flux based on the resolved temperature gradient is relatively low compared to the laminar counterpart but increases with the turbulent intensity. For the CMC cells immediately adjacent to the bluff body, the heat loss facilitates the occurrences of extinction and re-ignition. It has a significant influence on the mean flame structures, which is directly linked to the changes of the conditional scalar dissipation near the wall. Furthermore, the degree of local and instantaneous extinction measured by conditional reactedness at stoichiometry is intensified due to the wall heat loss. However, the wall heat loss shows a small impact on the lift-off near the bluff body surface.

## Acknowledgment

This work was completed under the financial support from the Engineering and Physical Sciences Research Council (EPSRC) and Rolls Royce Group in UK and start-up grant from National University of Singapore (R-265-000-604-133). Professor Epaminondas Mastorakos from University of Cambridge is gratefully acknowledged for helpful discussions.

## References

- Poinsot, T., and Veynante, D., 2005, *Theoretical and Numerical Combustion*, R.T. Edwards, Philadelphia, PA.
- Ju, Y., and Maruta, K., 2012, "Microscale Combustion: Technology Development and Fundamental Research," *Prog. Energy Combust. Sci.*, **37**(6), pp. 669–715.
- Kaisare, N. S., and Vlachos, D. G., 2012, "A Review on Microcombustion: Fundamentals, Devices and Applications," *Prog. Energy Combust. Sci.*, **38**(3), pp. 321–359.
- Lefebvre, A. H., 1999, *Gas Turbine Combustion*, 2nd ed., Taylor & Francis, London.
- Drysdale, D., 1999, *An Introduction to Fire Dynamics*, 3rd ed., Wiley, Chichester, UK.
- Karman, T. V., and Millan, G., 1953, "Thermal Theory of a Laminar Flame Front Near a Cold Wall," *Proc. Combust. Inst.*, **4**(1), pp. 173–177.
- Adamczyk, A., and Lavoie, G., 1978, "Laminar Head-On Flame Quenching—A Theoretical Study," *SAE Paper No. 780969*.
- Carrier, G. F., 1979, "Nonisenthalpic Interaction of a Planar Premixed Laminar Flame With a Parallel End Wall," *SAE Paper No. 790245*.
- Westbrook, C. K., Adamczyk, A. A., and Lavoie, G. A., 1981, "A Numerical Study of Laminar Flame Wall Quenching," *Combust. Flame*, **40**, pp. 81–99.
- Hocks, W., Peters, N., and Adomeit, G., 1981, "Flame Quenching in Front of a Cold Wall Under Two-Step Kinetics," *Combust. Flame*, **41**, pp. 157–170.
- Egolfopoulos, F. N., Zhang, H., and Zhang, Z., 1997, "Wall Effects on the Propagation and Extinction of Steady, Strained, Laminar Premixed Flames," *Combust. Flame*, **109**(1–2), pp. 237–252.
- Zhang, H., and Chen, Z., 2013, "Effects of Heat Conduction and Radical Quenching on Premixed Stagnation Flame Stabilized by a Wall," *Combust. Theory Modell.*, **17**(4), pp. 682–706.
- Vlachos, D. G., Schmidt, L. D., and Aris, R., 1993, "Ignition and Extinction of Flames Near Surfaces: Combustion of  $H_2$  in Air," *Combust. Flame*, **95**(3), pp. 313–335.
- Nakamura, H., Fan, A., Minamizono, H., Maruta, K., Kobayashi, H., and Niioka, T., 2009, "Bifurcations of Stretched Premixed Flame Stabilized by a Hot Wall," *Proc. Combust. Inst.*, **32**(1), pp. 1367–1374.
- Altay, H. M., Kedia, K. S., Speth, R. L., and Ghoniem, A. F., 2010, "Two-Dimensional Simulations of Steady Perforated-Plate Stabilized Premixed Flames," *Combust. Theor. Model.*, **14**(1), pp. 125–154.
- Mallens, R. M. M., and Goey, L. P. H. D., 1998, "Flame Cooling by a Curved Burner Wall," *Int. J. Heat Mass Transfer*, **41**(4–5), pp. 699–707.
- Oijen, J. A., and Goey, L. P. H., 2000, "Modelling of Premixed Laminar Flames Using Flamelet-Generated Manifolds," *Combust. Sci. Technol.*, **161**(1), pp. 113–137.
- Popp, P., and Baum, M., 1997, "Analysis of Wall Heat Fluxes, Reaction Mechanisms, and Unburnt Hydrocarbons During the Head-On Quenching of a Laminar Methane Flame," *Combust. Flame*, **108**(3), pp. 327–348.
- Jiménez, J., 2013, "Near-Wall Turbulence," *Phys. Fluids*, **25**(10), pp. 101302–101330.
- Grötzbach, G., 1987, "Direct Numerical and Larger Eddy Simulation of Turbulent Channel Flows," *Encyclopedia of Fluid Mechanics*, West Orange, NJ, pp. 1337–1391.
- Schmitt, P., Poinsot, T., Schuermans, B., and Geigle, K. P., 2007, "Large-Eddy Simulation and Experimental Study of Heat Transfer, Nitric Oxide Emissions and Combustion Instability in a Swirled Turbulent High-Pressure Burner," *J. Fluid Mech.*, **507**, pp. 17–46.
- Bray, K. N. C., and Peters, N., 1994, "Laminar Flamelets in Turbulent Flames," *Turbulent Reacting Flows*, P. A. Libby and F. Williams, eds., Academic, New York.
- Hergart, C., and Peters, N., 2001, "Applying the Representative Interactive Flamelet Model to Evaluate the Potential Effect of Wall Heat Transfer on Soot Emissions in a Small-Bore Direct-Injection Diesel Engine," *ASME J. Eng. Gas Turbines Power*, **124**(4), p. 10421052.
- Song, L., and Abraham, J., 2004, "A Wall-Modified Flamelet Model for Diesel Combustion," *SAE Paper No. 2004-01-0103*.
- Kim, G., Kang, S., Kim, Y., and Lee, K.-S., 2008, "Conditional Moment Closure Modeling for a Three-Dimensional Turbulent Non-Premixed Syngas Flame With a Cooling Wall," *Energy Fuels*, **22**(6), pp. 3639–3648.
- Paola, G. D., Mastorakos, E., Wright, Y. M., and Boulouchos, K., 2008, "Diesel Engine Simulations With Multi-Dimensional Conditional Moment Closure," *Combust. Sci. Technol.*, **180**(5), pp. 883–899.
- Kariuki, J., Dawson, J. R., and Mastorakos, E., 2012, "Measurements in Turbulent Premixed Bluff Body Flames Close to Blow-Off," *Combust. Flame*, **159**(8), pp. 2589–2607.
- Cavaliere, D., Kariuki, J., and Mastorakos, E., 2013, "A Comparison of the Blow-Off Behaviour of Swirl-Stabilized Premixed, Non-Premixed and Spray Flames," *Flow, Turbul. Combust.*, **91**(2), pp. 347–372.
- Zhang, H., and Mastorakos, E., 2016, "Prediction of Global Extinction Conditions and Dynamics in Swirling Non-Premixed Flames Using LES/CMC Modelling," *Flow, Turbul. Combust.*, **96**(4), pp. 863–889.
- Fureby, C., 1996, "On Subgrid Scale Modeling in Large Eddy Simulations of Compressible Fluid Flow," *Phys. Fluids*, **8**(5), pp. 1301–1429.
- Pera, C., Réveillon, J., Vervisch, L., and Domingo, P., 2006, "Modeling Subgrid Scale Mixture Fraction Variance in LES of Evaporating Spray," *Combust. Flame*, **146**(4), pp. 635–648.
- Garmory, A., and Mastorakos, E., 2011, "Capturing Localised Extinction in Sandia Flame F With LES-CMC," *Proc. Combust. Inst.*, **33**(1), pp. 1673–1680.
- Pierce, C. D., and Moin, P., 1998, "A Dynamic Model for Subgrid-Scale Variance and Dissipation Rate of a Conserved Scalar," *Phys. Fluids*, **10**(12), pp. 3041–3044.
- Zhang, H., Garmory, A., Cavaliere, D. E., and Mastorakos, E., 2014, "Large Eddy Simulation/Conditional Moment Closure Modeling of Swirl-Stabilized Non-Premixed Flames With Local Extinction," *Proc. Combust. Inst.*, **35**(2), pp. 1167–1174.
- Garmory, A., and Mastorakos, E., 2014, "Numerical Simulation of Oxy-Fuel Jet Flames Using Unstructured LES-CMC," *Proc. Combust. Inst.*, **35**(2), pp. 1207–1214.
- Clearly, M., and Kent, J., 2005, "Modelling of Species in Hood Fires by Conditional Moment Closure," *Combust. Flame*, **143**(4), pp. 357–368.
- Siwaborwon, P., and Kronenburg, A., 2013, "Conservative Implementation of LES-CMC for Turbulent Jet Flames," *High Performance Computing in Science and Engineering '12*, Nagel, W., Kröner, D., and Resch, M., eds., Springer, Berlin, pp. 159–173.
- Zhang, H., and Mastorakos, E., 2017, "Modelling Local Extinction in Sydney Swirling Non-Premixed Flames With LES/CMC," *Proc. Combust. Inst.*, **36**(2), pp. 1669–1676.
- Brien, O. E., and Jiang, T. L., 1991, "The Conditional Dissipation Rate of an Initially Binary Scalar in Homogeneous Turbulence," *Phys. Fluids*, **3**(12), pp. 3121–3123.
- Triantafyllidis, A., and Mastorakos, E., 2010, "Implementation Issues of the Conditional Moment Closure Model in Large Eddy Simulations," *Flow, Turbul. Combust.*, **84**(3), pp. 481–512.
- Navarro-Martinez, S., Kronenburg, A., and Mare, F. D., 2005, "Conditional Moment Closure for Large Eddy Simulations," *Flow, Turbul. Combust.*, **75**(1–4), pp. 245–274.

- [42] Beer, J. M., and Chigier, N. A., 1971, *Combustion Aerodynamics*, Applied Science Publishers, London.
- [43] Brown, P. N., and Hindmarsh, A. C., 1989, "Reduced Storage Matrix Methods in Stiff ODE Systems," *J. Appl. Math. Comput.*, **31**, pp. 40–91.
- [44] Sung, C. J., Law, C. K., and Chen, J. Y., 1998, "An Augmented Reduced Mechanism for Methane Oxidation With Comprehensive Global Parametric Validation," *Proc. Combust. Inst.*, **27**(1), pp. 295–304.
- [45] Cavaliere, D. E., 2013, "Blow-Off in Gas Turbine Combustors," *Ph.D. thesis*, University of Cambridge, Cambridge, UK.
- [46] Wang, Yi, and Arnaud Trouvé. "Direct numerical simulation of nonpremixed flame-wall interactions." *Combustion and flame* 144.3 (2006): 461–475.
- [47] Lataillade, A. D., Dabireau, F., Cuenot, B., and Poinot, T., 2002, "Flame/Wall Interaction and Maximum Wall Heat Fluxes in Diffusion Burners," *Proc. Combust. Inst.*, **29**(1), pp. 775–779.
- [48] Masri, A. R., Dibble, R. W., and Barlow, R. S., 1996, "The Structure of Turbulent Nonpremixed Flames Revealed by Raman-Rayleigh-LIF Measurements," *Prog. Energy Combust. Sci.*, **22**(4), pp. 307–362.
- [49] Kariuki, J., 2012, *Turbulent Premixed Flame Stabilization and Blow-Off*, University of Cambridge, Cambridge, UK.